Localized fault slip to the trench in the 2010 Maule, Chile Mw = 8.8 earthquake from joint inversion of high-rate GPS, teleseismic body waves, InSAR, campaign GPS, and tsunami observations

Han Yue, Thorne Lay, Luis Rivera, Chao An, Christophe Vigny, Xiaopeng Tong, Juan Carlos Báez Soto

AGU PUBLICATIONS

JGR

Journal of Geophysical Research: Solid Earth

RESEARCH ARTICLE
10.1002/2014JB011340

Key Points:
- The slip distribution of the 2010 Maule earthquake is determined
- Joint inversion of seismic, geodetic, and tsunami data resolves the slip
- Large slip extends to the trench in two locations along the rupture

Supporting Information:
- Readme
- Text S1
- Text S2

Correspondence to:
T. Lay,
tlay@ucsc.edu

Citation:
Yue, H., T. Lay, L. Rivera, C. An, C. Vigny, X. Tong, and J. C. Báez Soto (2014), Localized fault slip to the trench in the 2010 Maule, Chile M_w = 8.8 earthquake from joint inversion of high-rate GPS, teleseismic body waves, InSAR, campaign GPS, and tsunami observations, *J. Geophys. Res. Solid Earth*, *119*, 7786–7804, doi:10.1002/2014JB011340.

Received 31 MAY 2014
Accepted 23 SEP 2014
Accepted article online 27 SEP 2014
Published online 25 OCT 2014

Localized fault slip to the trench in the 2010 Maule, Chile M_w = 8.8 earthquake from joint inversion of high-rate GPS, teleseismic body waves, InSAR, campaign GPS, and tsunami observations

Han Yue[1], Thorne Lay[1], Luis Rivera[2], Chao An[3], Christophe Vigny[4], Xiaopeng Tong[5], and Juan Carlos Báez Soto[6]

[1]Department of Earth and Planetary Sciences, University of California Santa Cruz, Santa Cruz, California, USA, [2]Institut de Physique du Globe de Strasbourg, Université de Strasbourg/CNRS, Strasbourg, France, [3]School of Civil and Environmental Engineering, Cornell University, Ithaca, New York, USA, [4]Laboratoire de Géologie, Ecole Normale Supérieure, CNRS, Paris, France, [5]Scripps Institution of Oceanography, University of California San Diego, La Jolla, California, USA, [6]Centro Sismológico Nacional, Universidad de Chile, Santiago, Chile

Abstract The 27 February 2010, M_w 8.8 Maule earthquake ruptured ~500 km along the plate boundary offshore central Chile between 34°S and 38.5°S. Establishing whether coseismic fault offset extended to the trench is important for interpreting both shallow frictional behavior and potential for tsunami earthquakes in the region. Joint inversion of high-rate GPS, teleseismic body waves, interferometric synthetic aperture radar (InSAR), campaign GPS, and tsunami observations yields a kinematic rupture model with improved resolution of slip near the trench. Bilateral rupture expansion is resolved in our model with relatively uniform slip of 5–10 m downdip beneath the coast and two near-trench high-slip patches with >12 m displacements. The peak slip is ~17 m at a depth of ~15 km on the central megathrust, located ~200 km north from the hypocenter and overlapping the rupture zone of the 1928 M ~8 event. The updip slip is ~16 m near the trench. Another shallow near-trench patch is located ~150 km southwest of the hypocenter, with a peak slip of 12 m. Checkerboard resolution tests demonstrate that correctly modeled tsunami data are critical to resolution of slip near the trench, with other data sets allowing, but not requiring slip far offshore. Large interplate aftershocks have a complementary distribution to the coseismic slip pattern, filling in gaps or outlining edges of large-slip zones. Two clusters of normal faulting events locate seaward along the plate motion direction from the localized regions of large near-trench slip, suggesting that proximity of slip to the trench enhanced extensional faulting in the underthrusting plate.

1. Introduction

On 27 February 2010, the devastating Maule earthquake (M_w 8.8, M_s 8.3, seismic moment $M_0 = 1.86 \times 10^{22}$ Nm, http://www.globalcmt.org/) struck the coastal region of central Chile. The epicenter (36.29°S, 73.24°W, 06:34:08 UTC http://www.sismologia.cl/) was ~330 km southwest of Santiago. The rupture extended ~250 km to the NNE and ~250 km to the SSW, spanning ~500 km along strike from 34°S to 38.5°S. The earthquake generated a damaging tsunami, with 29 m maximum run-up water height reported at Constitución (http://www.ngdc.noaa.gov/hazard/tsu.shtml). The ground shaking and tsunami together caused more than 500 fatalities and estimated damage of $30B.

The 2010 Maule earthquake occurred on the plate boundary megathrust fault in the subduction zone where the Nazca plate is underthrusting the South American plate at a convergence rate of ~66 mm/yr [*Angermann et al.*, 1999]. In the last century, the megathrust north of the 2010 Maule event ruptured in 1906 (M ~8.4) and 1985 (M_w 7.8), and the 2010 rupture overlaps the 1928 (M ~8) rupture zone (Figure 1) [*Beck et al.*, 1998]. The megathrust to the south ruptured in the immense 1960 M_w 9.5 event [e.g., *Lay et al.*, 1982], with some overlap of the 2010 rupture with the northernmost end of the 1960 rupture zone. The megathrust region between Concepción and Constitución was recognized as a seismic gap, with the last previous rupture being in 1835 [e.g., *Compte et al.*, 1986; *Nishenko*, 1991; *Moreno et al.*, 2009; *Lay*, 2011; *Lorito et al.*, 2011]. The preshock slip-deficit pattern had been investigated by GPS observations [*Moreno et al.*, 2010] and indicated that the plate interface along the 2010 rupture was particularly strongly locked (>75%) in patches extending from 34°S–35°S to 35.5°S–37.5°S.

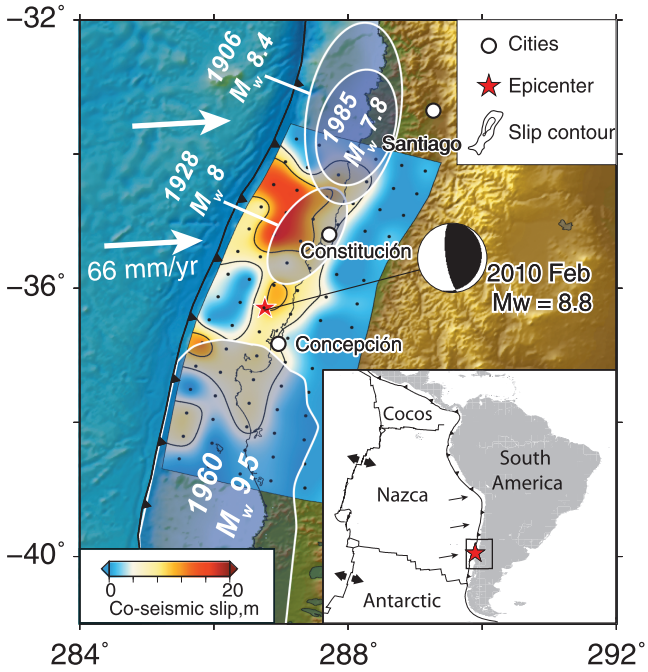

Figure 1. The 27 February 2010 M_w 8.8 Maule, Chile earthquake rupture zone and regional plate tectonic setting. The inset map indicates the Nazca plate subducting beneath the South American plate along the Chile trench. The relative plate motion, referenced to the South American plate, is marked with black arrows. The Chile trench is marked with a barbed line. The epicenter of the 2010 Maule event is indicated with a red star. The box identifies the region that is enlarged in the main map. The main map shows the Global Centroid-Moment Tensor best double-couple solution for the 2010 Maule event. The final slip distribution is shown with a blue-red-scaled contour map with 5 m and 10 m slip contour lines. Center locations of each subfault used in the inversion are marked with black dots. The estimated rupture areas of the 1906, 1928, 1960, and 1985 events are plotted with blue-filled patches, with the year and magnitude labeled. The location of the trench is indicated with the barbed curve. The relative plate motion between the Nazca and South American plates is indicated with white arrows. Major cities, Concepción, Constitución, and Santiago, are marked with white-filled circles.

The 2010 Maule main shock coseismic slip pattern has been investigated in numerous studies. Most indicate an asymmetric bilateral rupture, with larger slip in the NNE direction. *Lay et al.* [2010] and *Koper et al.* [2012] used teleseismic body and surface waves to resolve a bilateral rupture model that expanded ~450 km along strike. Significant near-trench slip (>10 m) is found in northern and southern patches in their models, but it is recognized that the teleseismic body wave data do not unambiguously resolve the shallow slip. *Tong et al.* [2010], *Pollitz et al.* [2011], *Vigny et al.* [2011], *Lin et al.* [2013], and *Moreno et al.* [2012] used geodetic observations including InSAR data, coastal leveling, campaign GPS static offsets, and high-rate (hr-GPS) time series to investigate the coseismic slip distribution. The along-strike-slip distributions in these models are generally similar, with bilateral rupture expanding ~500 km along strike, but the slip amount and along-dip slip distribution vary among the geodesy-based inversions, largely as a result of nonuniform spatial sampling of different data types. Most of these models indicate little slip near the trench, with the exception that *Moreno et al.* [2012] found ~5 m of slip near the trench updip of the northern slip patch in their model. *Vigny et al.* [2011] suggested that the rupture of the 2010 Maule event likely reached to shallow depth, possibly extending to the trench, but their data could not resolve this. *Delouis et al.* [2010] developed a coseismic rupture model using hr-GPS, InSAR images for a descending orbit, and teleseismic body and surface waves. In their study ~5 m of slip is also found near the trench updip of the northern rupture patch. *Lorito et al.* [2011] and *Fujii and Satake* [2013] investigated the coseismic slip pattern by inverting the tsunami and costal geodetic data sets. Their rupture model resembles the geodesy-based solutions, with little significant slip resolved near the trench.

The basic rupture pattern of the 2010 Maule event is generally consistent across all of the studies mentioned above. The along-strike-slip distribution is particularly well constrained by the on-land observations from Phased Array type L-band Synthetic Aperture Radar (PALSAR) InSAR phase data on board the ALOS satellite [*Shimada et al.*, 2010]. However, the along-dip slip distribution is less well resolved, with the amount of slip near the trench being uncertain. This is not an uncommon situation for older great events for which far fewer data are available, and the general tendency has been to assume that coseismic slip during great megathrust events does not extend to the toe of the sedimentary prism. However, the 2011 Tohoku, Japan M_w 9.0 event has demonstrated that large slip on the megathrust can drive slip to the trench, so this assumption is not secure [e.g., *Fujiwara et al.*, 2011; *Kido et al.*, 2011; *Lay et al.*, 2011b; *Kozdon and Dunham*, 2014]. The apparent lack of slip extending to the trench for the 2010 Maule event has been interpreted in the context of frictional models for the megathrust and mechanical analysis of the forearc structure and morphology [e.g., *Cubas et al.*, 2013], and

such interpretations directly depend on confidence in the absence of coseismic slip. The importance of evaluating the potential for near-trench tsunami earthquakes updip of great earthquake slip zones was demonstrated by the 2010 Mentawai M_w 7.8 tsunami earthquake, which ruptured updip of the 2007 M_w 8.5 Indonesia earthquake and produced a catastrophic tsunami [e.g., *Lay et al.*, 2011a; *Yue et al.*, 2014].

It is known that slip at shallow depth near the trench is poorly resolved by onshore geodetic data [e.g., *Miyazaki et al.*, 2011; *Ohta et al.*, 2012], and that typical regularization of geodetic inversions penalizes distant slip such that resulting models intrinsically tend to have reduced slip updip near the trench. Teleseismic observations are also usually unable to stably resolve near-trench slip, due to low resolution for shallow, nearly horizontal shear dislocations for both body and surface waves. It has been demonstrated that joint inversion of hr-GPS and teleseismic data sets can improve resolution of near-trench slip because it exploits the dynamic wave motions in the GPS recordings [*Yue and Lay*, 2013]; however, near-trench slip is still relatively less well resolved compared with downdip slip. Offshore geodetic measurements are of great value [e.g., *Kido et al.*, 2011] but remain unavailable for most subduction zones. In contrast to land-based geodetic and seismic data sets, tsunami observations can provide good resolution of near-trench slip, due to both the strong tsunami generation by shallow rupture and the good spatial resolution provided by slow tsunami waves [e.g., *Maeda et al.*, 2011; *Yamazaki et al.*, 2011; *Satake et al.*, 2013], but accurate propagation corrections are needed, and the long wavelengths involved do limit detailed slip characterization.

We have previously incorporated tsunami modeling into our source inversions using iterative inversion of seismic and geodetic data and forward modeling of tsunami observations, adjusting poorly constrained inversion parameters to achieve compatible models [*Yamazaki et al.*, 2011; *Yue et al.*, 2014]. Multiple iterations are typically required to achieve a model consistent with all observations. In this study, tsunami observations are explicitly included in joint linearized inversion with seismic and geodetic data to exploit the information of all data sets and to achieve stable inversion results. We find that the joint inversion improves the resolution of the slip near the trench as well as across the entire fault plane. Localized regions of large slip are found to extend to the trench, while other regions had no coseismic slip at shallow depths, updip of deeper slip zones.

2. Data and Methods

2.1. Fault Parameterization

The rupture model is initially parameterized with a dip-varying fault surface with a scale of 600×240 km^2. The fault plane is discretized into 15 subfaults along strike and 6 along dip, with the dimension of each subfault being 40×40 km^2. The hypocenter (36.29°S, 73.24°W) is located on the eighth subfault-center node along strike and third node along dip. Then the rectangular fault plane is adapted to the 3-D slab interface model resolved from gravity observations (Figure 2) [*Tassara and Echaurren*, 2012], keeping the same subfault depths but shifting the horizontal coordinates. Parameters describing the geometry of each subfault, including local strike, dip, and length scale are adjusted from the curvature of the 3-D fault model. The adjusted dimensions of subfaults range from 38 to 45 km (Figure 2). Green's functions computed for slip vectors with rakes of 89° and 119° are used in a nonnegative inversion, allowing subfault subevent rake to vary within $104 \pm 15°$. The central rake value is taken from the W-phase best double-couple solution. The range of rake variation (30°) is smaller than the 90° range allowed in our previous work, because we found that the tsunami waves, being primarily sensitive to ocean floor uplift but not to rake, could yield unstable rake fluctuations in the joint inversions.

We adopt a multitime-window algorithm to parameterize the subfault source time function [*Hartzell and Heaton*, 1983], in which the source time function of each subfault is parameterized with a series of triangles with an initial time calculated for an assumed maximum rupture velocity. The algorithm of *Yue and Lay* [2013] is used to combine different data sets in a joint inversion. Data processing and Green functions computation for each data set are described in the following.

2.2. hr-GPS Data Set

Our 1 s sampled hr-GPS data set is essentially the same as described in detail and modeled in *Vigny et al.* [2011]. The original hr-GPS recordings were processed with TRACK software developed at the Massachusetts Institute of Technology (MIT). The processing used the LC combination and International Global Navigation Satellite Systems Service precise orbits, and we apply a smoothing filter on the backward solution to estimate

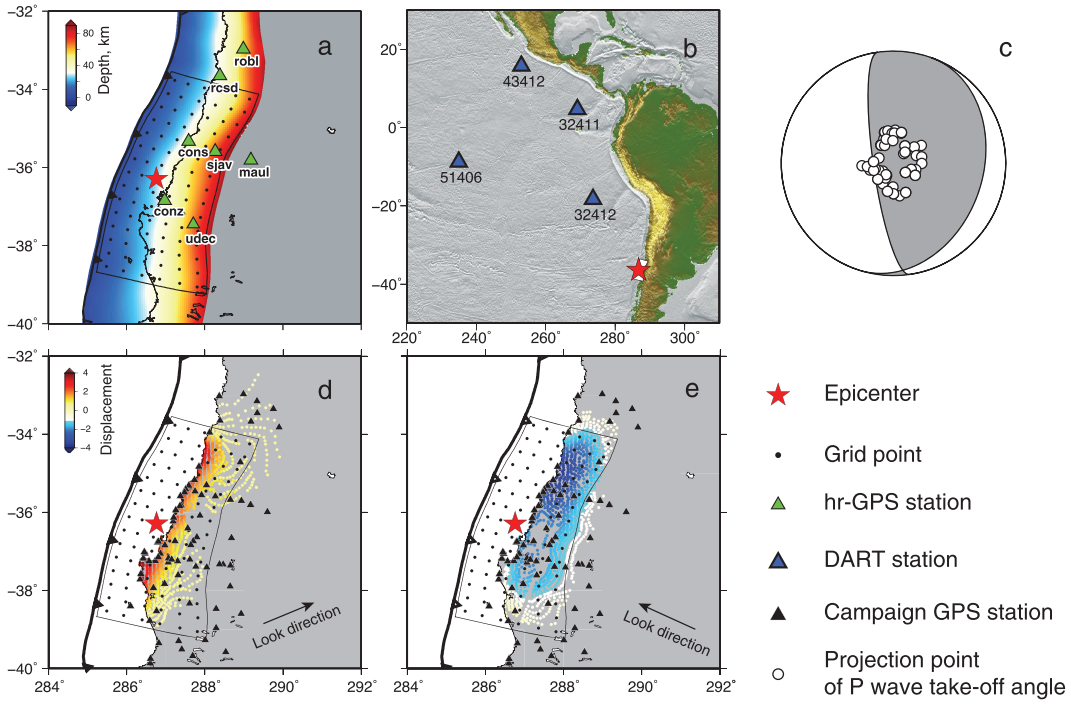

Figure 2. Rupture model parameterization and data sets used in the joint inversion. (a) Map of the rupture model grid, parameterized with 15 nodes along strike and 6 nodes along dip. The black polygon defines the fault model surface. Locations and geometry of each subfault are adapted to the 3-D plate boundary model [*Tassara and Echaurren*, 2012] shown with blue-red color scale. Approximate subfault dimensions are 40×40 km^2. Center locations of all subfaults are indicated with black dots. Locations of high-rate GPS stations are marked with green-filled triangles with station names. (b) Locations of four DART stations (blue-filled triangles), with station names indicated. Ocean bathymetry gradient is shown with a gray-scaled map. (c) The azimuths and take-off angles of teleseismic *P* and *SH* wave ground motion recordings used in our inversion are projected onto the lower hemisphere equal area stereographic projection along with *P* wave radiation nodes. (d and e) Sample points of ground displacements projected to the (line of sight) LOS direction of ascending and descending orbits. Displacements in LOS direction are shown by a blue-red color scale with the color bar shown on the top left of Figure 2d. The look direction is indicated with a black arrow. The location of 86 campaign GPS stations used in the joint inversion is plotted with black-filled triangles.

the atmospheric delays using 24 h data and fixing any noninteger biases to a constant value. TRACK computes a relative position with respect to a fixed reference station, and station SILL (70.739°W 29.255°S) was selected as the reference, because it is close enough to the hypocenter to ensure high accuracy of relative location, yet far away enough to avoid contamination of the dynamic responses at the stations close to the rupture. The processed hr-GPS records are essentially the relative position between each station and the reference station (SILL). Stations within 500 km epicentral distance are used in our joint inversion; more distant stations have low signal-to-noise ratios and intrinsic insensitivity to fault finiteness.

Three-component records of 7 h GPS stations (Figure 2a) are used in our joint inversion. Because TRACK computes relative position from a reference station, some coherent signal at 230–250 s is apparent at all stations (Figure 3), which is caused by the ground shaking from surface waves arriving at the reference station. To remove this coherent signal, we cut the hr-GPS records at 180 s, after the dynamic waves have passed the closer stations but not yet reached the reference station. The waveforms after 180 s at the seven stations are averaged to extract the common dynamic motions at the reference station. The stacked displacement is then removed from all traces, suppressing the coherent phases (Figure 3). We found this procedure more stable than explicitly predicting the SILL motions and differencing the signals.

To model the time-dependent near-field ground displacements recorded by hr-GPS, Green functions for the full dynamic and static elastic deformation field must be used. To exploit the short-period information for very near-field displacements, we apply a frequency-wave number (F-K) integration method that includes all near-field terms (Computer Programs in Seismology, Robert Herrmann) to compute Green's functions for five

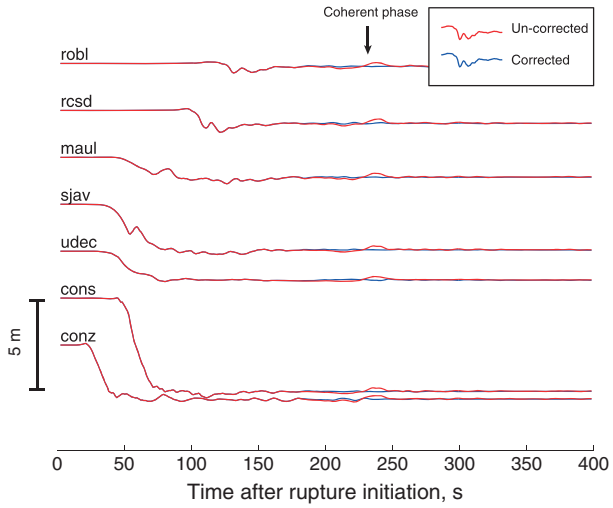

Figure 3. Time histories of the east-west (downward is westward) ground displacement components at 7 hr-GPS stations, referenced to station SILL, are plotted in red. A coherent feature, caused by arrival of surface waves at station SILL, is apparent at about 230 s in all records. The coherent signal was estimated by averaging signals for the seven records after their dynamic motions had ended (after 180 s). The coherent signal was then removed from all of the records, giving corrected waveforms plotted in blue.

nearby stations, *conz*, *cons*, *udec*, *sjav*, and *maul*. The F-K method accounts for both dynamic and static near-field ground displacements. The 1-D layered model for the Green's function computation is extracted from a local tomography model [*Haberland et al.*, 2009]. Parameters of the local 1-D model are listed in supporting information. A 300 s long time window is used for both data and Green functions, both of which are filtered with a 1 pass fourth order Butterworth low-pass filter with a corner frequency of 0.1 Hz. Because the data sample rate of station *udec* is 5 s, we apply a low-pass filter with a corner frequency of 0.06 Hz to both the records and Green's functions of that station to model the valid frequency content.

The 5 hr-GPS stations listed above locate within 500 km from all subfaults, and the flat-layered Earth model is sufficient to capture the first-order wave propagation behavior. For more distant stations *rcsd* and *robl*, Earth curvature is accounted for using Green functions calculated by mode summation for a spherical Earth model. We sum all modes for the Preliminary Reference Earth Model (PREM) up to 80 mHz [*Yue and Lay*, 2011]. PREM is not a realistic regional structure to capture the high-frequency wave propagation in continental lithosphere; thus, we apply a low-pass filter with lower corner frequency, at 0.06 Hz, to utilize the low-frequency energy in both data and Green functions for these two stations. This corner frequency proved effective for inverting hr-GPS records of the Tohoku earthquake [*Yue and Lay*, 2011].

2.3. Teleseismic Data Set

The teleseismic body wave data set is composed of 43 *P* wave and 18 *SH* wave ground displacement recordings (Figure 2c) from stations of the Federation of Digital Seismic Networks (FDSN), accessed through the Incorporated Research Institutions for Seismology (IRIS) data management center. The data set is selected from hundreds of available FDSN seismograms to ensure good azimuthal coverage and high signal-to-noise ratios for epicentral distances from 40° to 90°. Instrument responses are deconvolved to provide ground displacement with a band-pass filter having corner frequencies of 0.005 and 0.9 Hz. Long time windows of 180 s are used, starting 10 s prior to initial *P* or *SH* arrivals. The *P* wave signals provide information about seismic radiation for periods as short as several seconds but are depleted in shorter period energy due to the nature of the source process.

The teleseismic Green functions are generated using a reflectivity method that accounts for body wave interactions in 1-D layered structures on both source and receiver sides [*Kikuchi et al.*, 1993]. The same local source velocity model is used in the Green function's computation as that used in hr-GPS Green functions computation. A typical continental model is used for the receiver side. The same band-pass filter used for the data is applied to the Green functions.

2.4. InSAR Data Set

The InSAR data set used in this study is the same as described in detail in *Tong et al.* [2010], composed of 1080 samples of descending orbit and 821 samples of ascending orbit (Figures 2d and 2e). The InSAR sampling covers the full length of the fault plane and extends from the coastline to ~150 km inland. The combination of ascending and descending images provides observations of coseismic deformation in two directions, which

provides well-constrained slip distribution, especially for the along-strike distribution and the downdip slip termination [*Tong et al*., 2010].

The Green functions used to model the coseismic ground deformation for the InSAR modeling are computed from a FORTRAN code developed by *Wang et al*. [2003]. This uses an orthonormalization method [*Wang*, 1999] to compute static ground displacement fields for a rectangular dislocation source in layered media. The same local source velocity model used in hr-GPS and teleseismic Green's function computation, after removing the water layer, is adopted to compute the static ground displacements. Three-component ground displacements are computed and projected to the two line of sight (LOS) directions for each InSAR sample point. These data can be affected by early afterslip, but it appears this is a relatively minor source of error for this event [e.g., *Agurto et al*., 2012; *Bedford et al*., 2013].

2.5. Campaign GPS Data Set

Three-component coseismic ground displacement records from 82 campaign GPS stations are used in the joint inversion (Figure 2). The adopted campaign GPS data are the processed GPS solutions from *Vigny et al*. [2011], *Moreno et al*. [2012], and *Lin et al*. [2013]. The spatial distribution of campaign GPS stations covers a similar scale as the InSAR data set but with a sparser sampling. The Green functions for the campaign GPS data set are computed by the layered structure code of *Wang et al*. [2003] using the local 1-D model, the same as for InSAR modeling. Stations located within 400 km from the epicenter are selected from 167 available records to ensure validity of flat Earth model Green functions. These data can also be affected by early afterslip, but we again assume this is negligible.

2.6. Tsunami Data Set

Wave heights recorded at four NOAA DART (Deep ocean Assessment and Reporting of Tsunamis) ocean bottom pressure stations are used in our joint inversion (Figure 2b). Detided wave height recorded at 1 sample per minute is accessed from NOAA (http://ngdc.noaa.gov/hazard/dart/2010chile_dart.html).

Issues about linear inversion validity arise when including tsunami data in linearized finite-fault inversion, associated with nonlinear wave excitation and propagation in very shallow water. The nonlinear wave propagation makes it very challenging to model short-wavelength wave heights recorded near the coast, such as in tide-gauge recordings. However, for deep ocean wave height, such as the DART data, the scaling and superposition of tsunami waves intrinsic to a many-subfault model can be reasonably assumed to follow a linear relationship for the direct main tsunami pulse [e.g., *Satake et al*., 2013]. For the deep ocean records, modeling with linear and nonlinear codes produces very similar results for the main tsunami pulse dominated by long-wavelength arrivals, indicating that the nonlinear wave effects are not too important for the deep ocean recordings, as long as the more affected short-wavelength signals are delayed out of the time window by dispersion. In our inversions, the tsunami waveforms are windowed to include only the signal around the main arrival of each tsunami recording, omitting later reflections from the coast that are more sensitive to the nonlinearity of excitation and shallow water propagation affecting the short-wavelength signals.

2.7. Tsunami Green Functions Generation and Correction

The tsunami Green functions are computed with COMCOT (Cornell Multigrid Coupled Tsunami Model code; http://ceeserver.cee.cornell.edu/pll-group/comcot.htm), a linear nondispersive code that solves the shallow water wave equations. We use the 1 arc min ocean bathymetry model resampled from GEBCO_08 (http://www.gebco.net/data_and_products/gridded_bathymetry_data/). The Green functions for each subfault are for vertical ground displacements calculated by the Okada model [*Okada*, 1992]. The vertical displacement of the ocean floor is taken as the initial ocean surface height, and then COMCOT solves for the resulting wave propagation. Horizontal displacements in the presence of irregular bathymetry also produce ocean floor uplift [*Tanioka and Satake*, 1996]. We use the method of *Tanioka and Satake* [1996] to calculate the coseismic horizontal displacements from the Okada model, performing a vector product with the ocean bathymetry normal vector to scale up the uplift-based tsunami Green functions. The horizontal displacements contribute 10–20% of the total uplift. Coseismic displacements calculated for the source velocity model using *Wang et al*. [2003] were also used to further scale up the Green functions to simulate ground deformation consistent with layered

models used for the hr-GPS, campaign GPS and InSAR Green's functions. For our velocity structure this correction is just a scale factor, as the frequency dependence is very small.

It has been observed that for the 2011 Tohoku earthquake and other large events, modeled tsunami based on different computational methods tend to arrive earlier than observed tsunami, with about a ~1% velocity discrepancy [*Simons et al*., 2011; *Yamazaki et al*., 2012]. This can amount to as much as 10 min error when propagating across the Pacific Ocean [*Watada et al*., 2014] and clearly presents a limitation for resolving slip distribution for large megathrust earthquakes. The causes of this mismodeling have been investigated by *Tsai et al*. [2013] and *Watada et al*. [2014]. It appears that most of the velocity discrepancy results from neglecting the contributions from coupling between the gravity of the water column and the elasticity of the ocean floor. There is also a contribution from water density increase with depth, which is usually ignored. In addition, dispersion effects of the oceanic waveguide do play an important role in short-period tsunami wave propagation, and some tsunami modeling codes do not account for this. The combination of the three sources of error requires correction of the tsunami dispersion curve in which $>1\%$ velocity correction is applied to all wave numbers [*Tsai et al*., 2013]. Application of these corrections can strongly suppress the tsunami traveltime discrepancies.

Because absolute timing is critical for our joint inversion, we apply corrections to our tsunami Green functions to ensure accurate propagation effects. Since our tsunami synthetics are generated with a nondispersive algorithm, all three corrections need to be applied to our Green functions data set. Our calculation of the corrected tsunami phase velocity, c, is given by

$$c = c_0 - c_1 - c_2 - c_3 \tag{1}$$

where

$$c_0 = \sqrt{gh} \tag{2}$$

$$c_1 = \sqrt{gh}\left[1 - \sqrt{\frac{\tanh(kh)}{kh}}\right] \tag{3}$$

$$c_2 \approx \sqrt{gh}\frac{(1-v)\rho g}{2\mu k} \tag{4}$$

$$c_3 \approx \sqrt{gh}\frac{\Delta\rho}{4\rho_{\text{avg}}} \tag{5}$$

For the shallow water equation c_0 is the nondispersive velocity, c_1 accounts for the nonshallow water dispersion [*Mei*, 1989], c_2 is caused by the water-column gravity and ocean floor elasticity coupling [*Tsai et al*., 2013], and c_3 is caused by the effect of water density gradient with depth [*Tsai et al*., 2013]. In these equations, h is the water depth, k is the wave number, $v = 0.3$, and $\mu = 73$ GPa are the Poisson's ratio and shear modulus of the elastic ocean floor. We used the elastic parameters of the PREM model averaged over the upper 500 km depth to approximate the penetration depth for tsunami waves with similar wavelength, which is higher than the shear modulus of 50 GPa used in *Tsai et al*. [2013]. The lower shear modulus tends to overcorrect the tsunami Green's functions, causing excessive phase delay, so we used the average shear modulus appropriate for the penetration depth of the coupled tsunami-elastic waves of our observed tsunami data. $\Delta\rho = 19$ kg/m^3 is the density variation of the water column, and $\rho_{\text{avg}} = 1036$ kg/m^3 is the average density of the water layer. To apply these corrections to the Green functions, these expressions in the wave number domain are converted to the frequency domain by the relationship $k = \omega/c \approx \omega/\sqrt{gh}$.

Note that c_1 and c_2 both depend on k or ω, indicating they are both dispersive. The c_1 term (shallow water wave equation dispersion) causes shorter period waves to travel slower, which is normal dispersion; however, the c_2 term (gravity-elasticity coupling) makes longer period waves travel slower because they couple more with ocean floor elasticity, producing reverse dispersion. The COMCOT Green functions provide a reference state for which all wave periods travel at the same velocity c_0 and capture the first-order propagation effects such as geometric spreading and focusing/defocusing. By applying corrections for each period we produce dispersed Green functions that have correct arrival times and wave shapes, assuming the propagation effects are linear, without changing the amplitude other than as a result of dispersion. Because the velocity corrections are small (1–3%) relative to the ocean bathymetry contrasts there should not be significant change in the geometric spreading at each period.

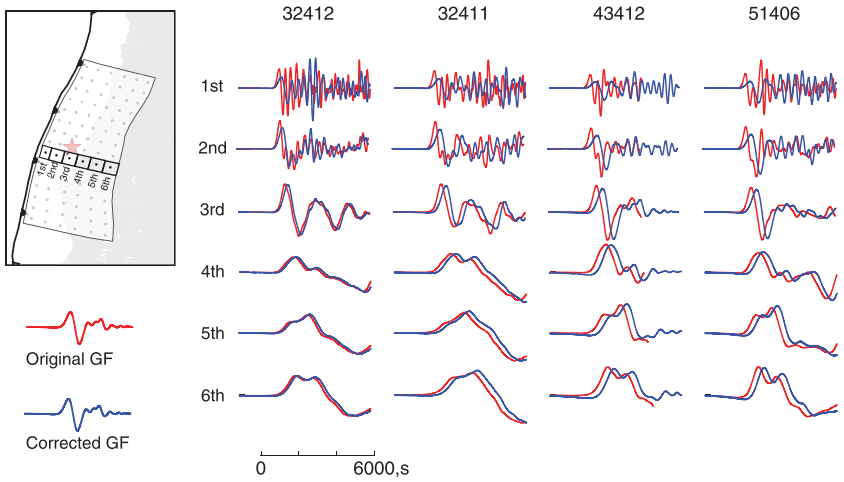

Figure 4. Initial dispersion-free and dispersion-corrected tsunami Green's functions are plotted in red and blue, respectively. The seventh column of subfaults in the finite-source model is selected to demonstrate the effect of the dispersive phase correction. The location and indexing of the subfaults is shown in the top left panel. The waveforms are ordered by subfault index in the vertical direction and epicentral distance in the horizontal direction. Subfault index and DART station name (see Figure 2b) are shown on the left and top of each row and column, respectively. The timescale is presented at the bottom. The phase correction, which is a cumulative effect of wave propagation, is more significant at larger distances. Dispersive effects are more obvious for updip subfaults, while for downdip subfaults the corrections behave more like a time shift.

Our phase correction procedure includes the following:

1. Calculate the bathymetry profile along the great circle through the smoothed ETOPO1 model, for each source-receiver pair. For the corrections we assume the tsunami propagates along the great circle, which could be biased by the near coast bathymetry gradient. However, all of our tsunami observations are in the deep ocean basin, and no source-receiver path approaches the continental boundary, thus the direct wave paths are little impacted by the near coast bathymetry gradient. In additions, the tsunami waves used in our study are very low frequency, associated with wavelengths of hundreds of kilometers, which are not sensitive to the detailed bathymetry along the path. Therefore, we used a smoothed bathymetry model to make corrections.
2. Discretize the path into n segments and calculate the nondispersive arrival time by $t_0 = \sum_{i=1}^{n} \frac{d_i}{\sqrt{gh_i}}$, where i is the index of each segment along the path. h_i is the associated bathymetry at each segment.
3. Fourier transform the original tsunami Green's function.
4. Calculate the dispersive velocity correction at each segment i using equations (2), (3), (4), and (5) for each frequency of the Green function spectrum:

$$c_i(\omega) = c_{i0} - c_{i1}(\omega) - c_{i2}(\omega) - c_{i3}$$

5. Calculate the corrected arrival time of each frequency by $t(\omega) = \sum_{i=1}^{n} \frac{d_i}{c_i(\omega)}$ and obtain the differential arrival time by $\Delta t_{(\omega)} = t_{(\omega)} - t_0$
6. Convert the differential arrival time to phase delays by $\Delta\varphi(\omega) = -2\pi i\omega\Delta t_{(\omega)}$, where $i = \sqrt{-1}$.
7. Apply the phase correction to each frequency of the Green functions and convert back to the time domain.

This phase correction is applied to each source-receiver pair. Examples of the original and corrected Green functions are shown in Figure 4. The corrected Green functions for shallow subfaults acquire a more dispersed shape, with low-frequency energy arriving earlier than high-frequency energy. This dispersive effect has significant effect on the waveforms of the Green's functions. Corrections for downdip Green functions provide more of a uniform waveform shift, due to weak excitation of short-period tsunami energy. Weak, early negative energy is apparent in the corrected Green's functions, caused by the reverse dispersion of gravity-elastic coupling as noted by *Watada et al*. [2014]. The corrections are larger for more distant stations, because the velocity corrections accumulate with distance.

These corrected tsunami Green function can now be directly used in our joint inversion using absolute time (as for the hr-GPS signals), without empirically (arbitrarily) adjusting the arrival times of tsunami synthetics as

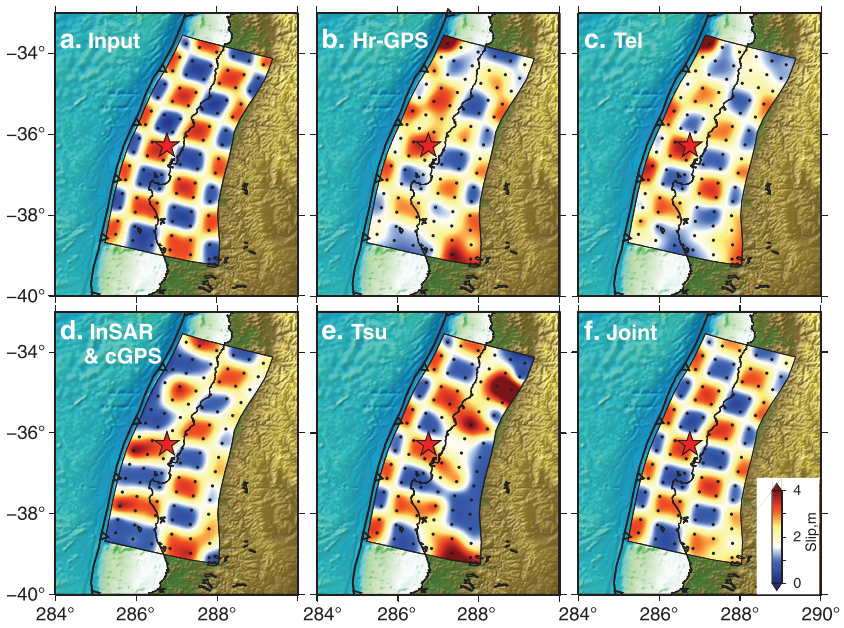

Figure 5. Checkerboard tests of inversions with all data sets separately and jointly. (a) The input model, with 2 m slip assigned to every other 2 × 2 subfault patch. Noise, rupture velocity uncertainties, and regularization are adopted in all inversions as discussed in the text. (b) Inversion of the hr-GPS data set resolves the central region of the slip pattern but has substantial distortion and overestimation of slip on more distant patches. (c) Inversion of the teleseismic data set has good downdip resolution but diminished resolution of shallow slip near the trench. (d) The InSAR and campaign GPS data sets provide good downdip resolution along the entire model, but the slip pattern near the trench is smeared from downdip. (e) The tsunami data set provides good resolution of near-trench slip but limited resolution of downdip rupture. (f) The joint inversion combines the complementary advantages of the data sets and allows accurate recovery of the input model.

has been done in previous studies. Earlier analyses of the tsunami signals for the 2010 Maule event have noted the issue of dispersion correction and bias in the absolute times due to ignoring elasticity of the underlying medium, but this is the first study to correct for all the known effects for a source inversion.

2.8. Checkerboard Test

Checkerboard tests are commonly used to investigate inversion stability and data resolution. Here we present checkerboard tests to evaluate intrinsic resolution provided by each type of data set and to explore the potential advantage of joint inversion. In our checkerboard tests the input model is specified with 3.86 m of slip (2 m of slip for each slip vector) for every other 2 × 2 subfault group (Figure 5a). A rupture velocity of 2.8 km/s is used to set the initial time of each subfault. Synthetics for all four data sets are generated with the same Green functions used in the inversion. A 10% level of white noise is added to all synthetics. In the inversion of checkerboard synthetics, we prescribed the rupture velocity to be 10% higher than the input rupture velocity and used relatively long (20 s) subfault source durations to capture the source duration of all subfaults. For the inversions of actual data, the rupture velocity may not be uniform and the precise rupture velocity is not well known, so we will similarly specify a high enough rupture velocity and long enough subfault source durations to avoid kinematically biasing the results [*Yue and Lay*, 2013]. Some regularization or smoothing is applied to the checkerboard inversions to stabilize the results, similar to what we apply to actual data.

We performed checkerboard inversions for all data sets separately and jointly. Representative results are shown in Figure 5. We have previously found that hr-GPS data provide good resolution and inversion stability if the station distribution is adequate [*Yue and Lay*, 2011, 2013]. For the 2010 Maule event, most hr-GPS stations are located north along the fault plane (Figure 3), such that the slip to the south is not well constrained (Figure 5b). In particular, slip on the southern half of the shallowest row is underestimated in the hr-GPS inversion while slip at the north and south corner is overestimated significantly. Generally, slip near the trench tends to be overestimated and smeared, and the along-strike patchiness is not well resolved. The teleseismic body wave data set has generally good resolution near the hypocenter (Figure 5c) but poor resolution overall. The teleseismic data set has a tendency to overestimate the slip (moment) when a long

source duration is allowed for each subfault. The InSAR and campaign GPS data set provides very good resolution for downdip slip (Figure 5d), as a result of the continuous data sampling on land. However, the static coastal geodetic data have very limited resolution of updip slip, with the shallow model contaminated by smearing from the second row. The resolution provided by the tsunami data set (Figure 5e) is opposite to that of the static coastal geodetic data set: the slip near the trench and in the top three rows is very well resolved, but there is poor resolution downdip beneath the land. The deeper slip does not produce much tsunami excitation. Joint inversion (Figure 5f) combines the advantage of all data sets and resolves both the slip pattern and slip amount very well over the entire fault plane.

For the joint inversion we are combining a mix of data that have explicit time-dependent sensitivity (teleseismic body waves, dynamic waves in the hr-GPS, and tsunami signals) with static offset information (static motions in the hr-GPS and InSAR). The kinematic model is directly constrained by the time-varying information, but is informed by the static information, which requires spatially consistent slip. We specify a maximum initial rupture velocity even while allowing flexibility in the time history via the multitime window algorithm. The initial rupture velocity is commonly estimated by determining inversion residual trade-off curves [e.g., *Yue et al*., 2013]. Here we used a trade-off curve for the joint inversion, finding a preferred initial rupture velocity of 2.6 km/s. This is compatible with earlier studies, which utilize rupture velocities in the range 2.0 to 3.0 km/s.

Relative weighting always presents an important issue for joint inversions. The hr-GPS and InSAR geodetic data sets provide error estimates for the data for each sample point that can weigh the covariance matrix of the Green functions. However, for the teleseismic and tsunami data sets, the most significant error comes from the uncertainty of the Green functions, making it hard to formally estimate the intrinsic error in the joint inversion problem. Our previous approach has been to normalize each data set by some measure of corresponding maximum amplitude and to test the data set weighting relative to the natural weighting (equal weighting of the normalized data sets) to seek a minimum residual. For the 2010 Maule event, we found that reasonable variation of relative weighting does not introduce significant changes of the slip pattern or data fitting, and we finally chose to assign all data sets natural weighting.

Regularization approaches are generally necessary in geophysical inversions, which are mostly underdetermined, to stabilize the inversion. In our previous joint inversion work, we have explored different levels of regularization seeking to match independent observations, such as ocean bottom displacements [*Yue and Lay*, 2011] or tsunami waves [*Yue et al*., 2014]. For the joint inversion of the 2010 Maule event, we found that the slip estimation across the fault plane is sufficiently well constrained that smoothing beyond the intrinsic grid parameterization is not necessary to stabilize the inversion result. For the large grid spacing of ~40 km used in this study, significant regularization is intrinsic to the model discretization. The basic assumption underlying a relatively sparse grid is that the slip heterogeneity within a subfault is accounted for by the time-varying source time function at each subfault. For joint inversion including long-wavelength tsunami waves, 40 km is an acceptable subfault scale and we find that further regularization by smoothing is not necessary, while if a smaller subfault size is adopted (~15 km), smoothing is needed to prevent unstable local peak slip. For smaller subfaults the tsunami Green functions computation becomes excessive, and issues of linearity of small subfault areas for broadband tsunami excitation become important. For our preferred inversion result, we use the 40 km grid spacing and no further regularization was applied; this leads to some roughness of the solution, but the model is not dominated by smoothing criteria, as is typically the case. Abrupt variation of slip between adjacent grid points can be viewed as an artifact of the somewhat coarse model discretization.

3. Results and Discussion

The preferred finite-fault model is shown in a fault plane view in Figure 6. The rupture has a bilateral propagation pattern that is dominated by a northern slip concentration, as in most previous studies. The northern slip distribution extends ~240 km along strike from the hypocenter, with large slip being located 120–200 km north of the hypocenter at ~16 km depth. Significant slip of up to ~16 m is located updip of the peak slip patch, extending to the trench toe. A southern slip patch extends ~200 km along strike from the hypocenter. The peak slip (~12 m) is located near the trench. The near-trench fault region updip from the hypocenter has little slip. No significant slip is found in the lower two rows of the model, which shows a consistent downdip slip limit to that resolved by InSAR data [*Tong et al*., 2010]. This downdip limit may be

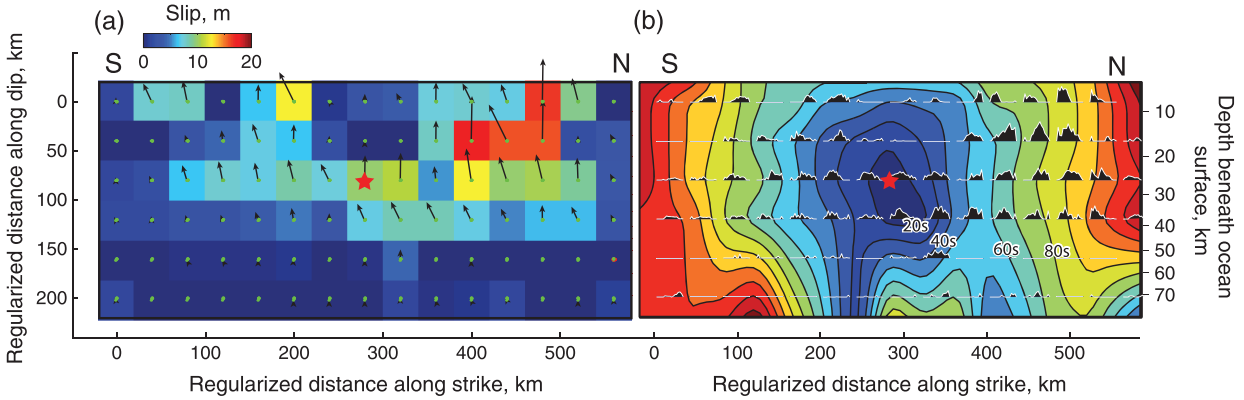

Figure 6. (a) Rupture-plane views of the slip distribution for the preferred model with a rupture velocity of 2.6 km/s. The scale of each subfault is adjusted to be 40×40 km^2. Center locations of each subfault are presented with green dots, with a black arrow presenting the rake direction scaled by the slip amount, which is also used for the color scale on the left. The largest slip occurred north of the hypocenter, with a maximum slip of ~17 m ~200 km north of the hypocenter in the second row. Updip from this large-slip region substantial slip (~16 m) occurred in the shallowest subfault extending to the trench. Rupture propagated to the south ~200 km, with averaged slip of ~8 m along the third row. The maximum slip of ~12 m in the south occurred near the trench. Slip updip from the hypocenter is insignificant. (b) Source time functions for each subfault node are shown as black-filled polygons. The centroid time of each node is contoured as the background colored map. Absolute depths are indicated on the right. In both panels, the hypocenter is indicated with a red-filled star.

controlled by the intersection of the upper plate Moho interface with the subduction slab, as has also been found for the 2012 Costa Rica $M_w = 7.6$ event [*Yue et al.*, 2013]. The cumulative seismic moment of our rupture model is 2.6×10^{22} Nm, giving a moment magnitude of $M_w = 8.88$; this is higher than the 1.9×10^{22} Nm value for the point-source GCMT solution. In part, this may represent the dip-varying geometry of the plate interface model and the use of a regional velocity model rather than PREM. Parameters of our inversion results are listed in the supporting information.

Fits of the joint inversion synthetics to all data sets are shown in Figure 7. Satisfactory matches of all five data sets are found. The residual of data fits to hr-GPS, InSAR, and campaign GPS data sets is several percent, consistent with the absolute errors in these geodetic-based observations of ~10 cm. The residual for teleseismic data fits is ~20%, which is a typical misfit of signal power achieved in teleseismic data fitting for joint inversions. The residual of tsunami waveform misfits is ~20% as well and comes primarily from the timing alignment of stations 32411 and 43412, for which the dominant peak is slightly shifted in the synthetics. With slip in the model already extending to the trench, no rupture further westward is viable to better match the initial arrival for these two stations, so it is likely there are some errors in the Green functions. This could be due to the propagation corrections applied to the tsunami Green functions or to errors in the bathymetric models.

The near-trench slip in the southern part of the rupture is not evident in most previous inversions of geodetic data. Contributions to data fits from this slip patch are insignificant for the hr-GPS, teleseismic, InSAR, and campaign GPS data sets, but the contribution is significant for some of the tsunami observations. The observed and modeled tsunami waveforms are plotted in Figure 7c, and the isolated contribution from the seven top left subfaults on the shallowest row of the model is plotted for comparison. The contributions from the seven subfaults to fits to the tsunami waves have significant azimuthal pattern, with the largest signals being for DART 51406. Because station 51406 is closer to the trench normal direction compared with other stations, the along-strike distribution of the seven subfaults produces more amplified tsunami waves relative to other stations. Station 51406 has two significant peaks, indicating two strong shallow slip patches in the 2010 Maule earthquake. The southern shallow slip accounts for the second peak. Because the other tsunami observations are from stations further to the northwest, the arrival from the southern shallow slip arrives late in the recordings, obscured by dispersion of earlier arriving signals. Lacking tsunami observations to the south, we cannot tightly bound the shallow slip in the south, but it is supported by the data at DART 51406.

To clarify the contribution to the joint inversion result from each data set, we produced four separate inversions for which one type of data (hr-GPS/teleseismic/InSAR+cGPS/tsunami) is left out (Figure 8). The same inversion parameters as used for the complete data inversion are held fixed in these tests, even though some instability can occur due to the enhanced null space of the solutions that could be mitigated by additional smoothing. This allows us to most clearly infer the data contributions to the joint model.

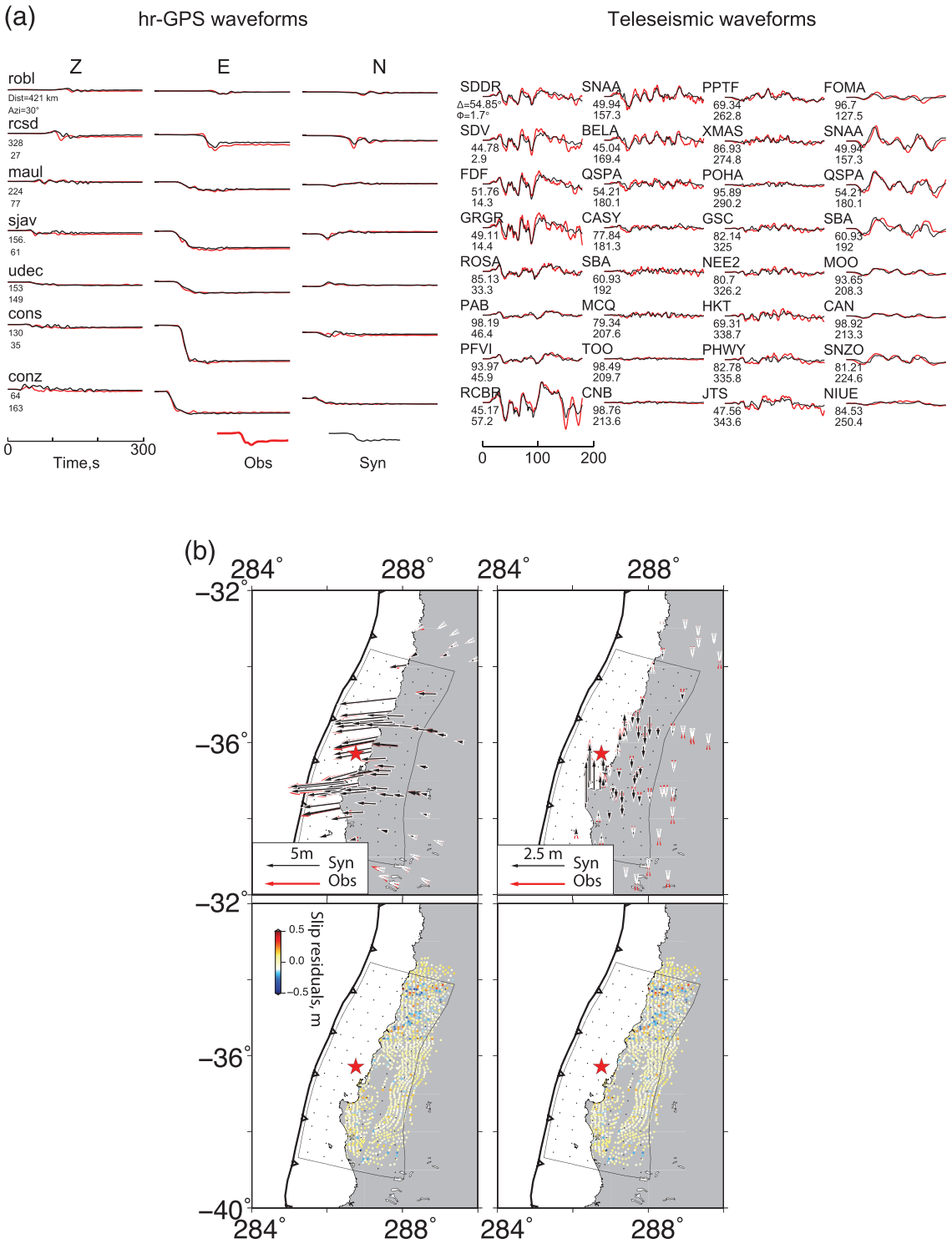

Figure 7. Data fits for the preferred joint inversion model. (a) Observed (red) and modeled (black) ground displacement signals for hr-GPS and selected teleseismic *P* waves and *S* waves. Station names, epicentral distances, and azimuth of each record are indicated. (b) Observed (red) and modeled (black) ground displacements are shown for horizontal (top left) and vertical (top right) displacements. Scale of displacements is shown in the bottom left corner. Residual displacements in LOS direction of each InSAR sample point are shown with a blue-red color scale for descending (bottom left) and ascending (bottom right) orbits, respectively. The epicenter is indicated with a red-filled star. Center locations of all subfaults are shown with black dots with the fault model boundary indicated with a black polygon. (c) Observed (red) and modeled (black) tsunami height at four DART stations. Station names and peak amplitude are shown. Waveform contributions from the first to seventh subfaults along strike in the first row, marked by orange rectangles in the left panel, are plotted in orange.

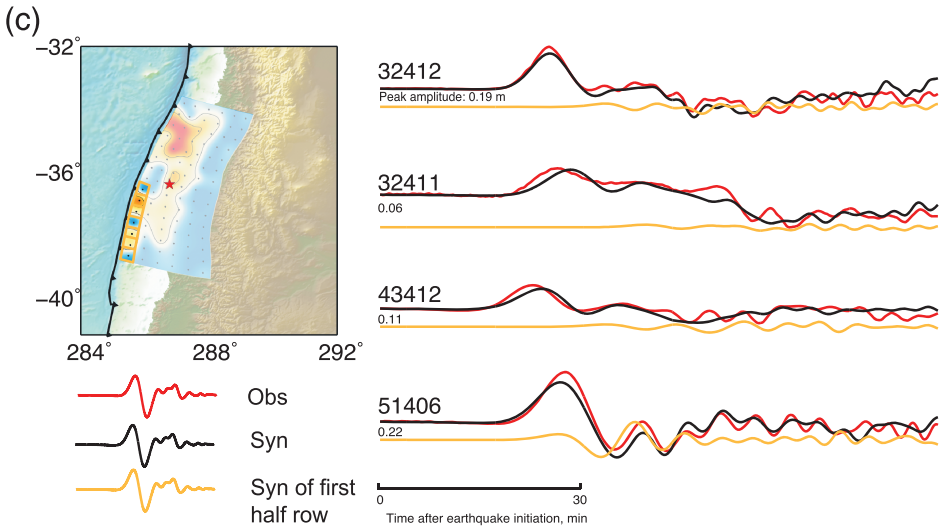

Figure 7. (continued)

The hr-GPS data set has dynamic and static ground displacement information that is also constrained by teleseismic and static geodetic observations. Therefore, the rupture pattern when hr-GPS data are omitted from the inversion is similar to that of the complete data set. The overall slip pattern when the teleseismic data set is omitted from the inversion also resembles the complete inversion, but the source time functions for the subfaults become unrealistically distributed and scattered. This indicates that the teleseismic data set has limited contribution to the overall slip distribution but provides important temporal information for the source time functions at each grid point due to its good time resolution.

When omitting the static geodetic data set, the rupture pattern is not well constrained. The inversion resolves the overall rupture distribution, but the inversion prefers isolated slip peaks. This indicates that the model resolution is significantly reduced when the static geodetic data set is excluded. For the 2010 Maule event, the InSAR and campaign GPS stations cover the full length of the rupture along strike, and that provides good

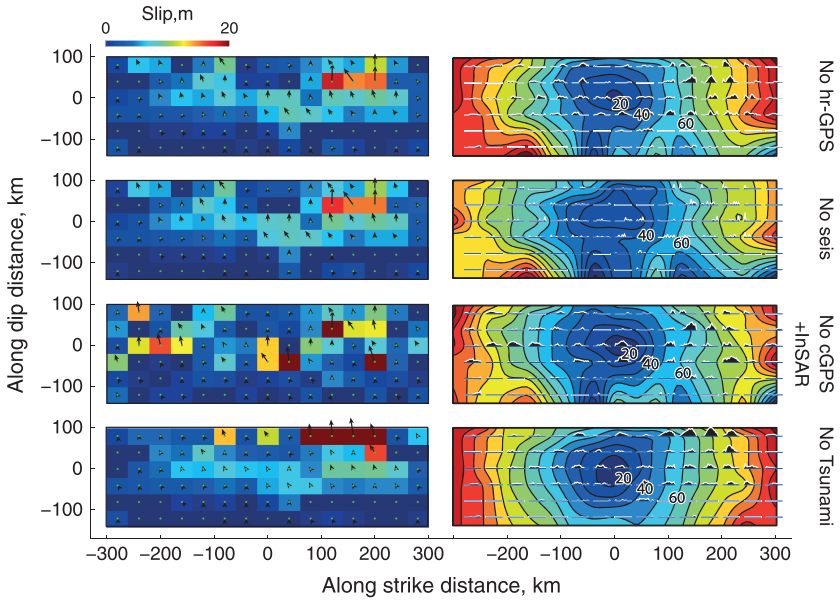

Figure 8. Fault plane displays for the inversions with omitted data sets. Final slip patterns are shown in the left column and source time functions and kinematic rupture expansion patterns are shown in the right column. Inversions without hr-GPS, teleseismic, InSAR+campaign GPS, or tsunami data sets are shown for the rows from top to bottom, respectively. Each inversion uses the same parameters for all included data as the complete joint inversion shown in Figure 6.

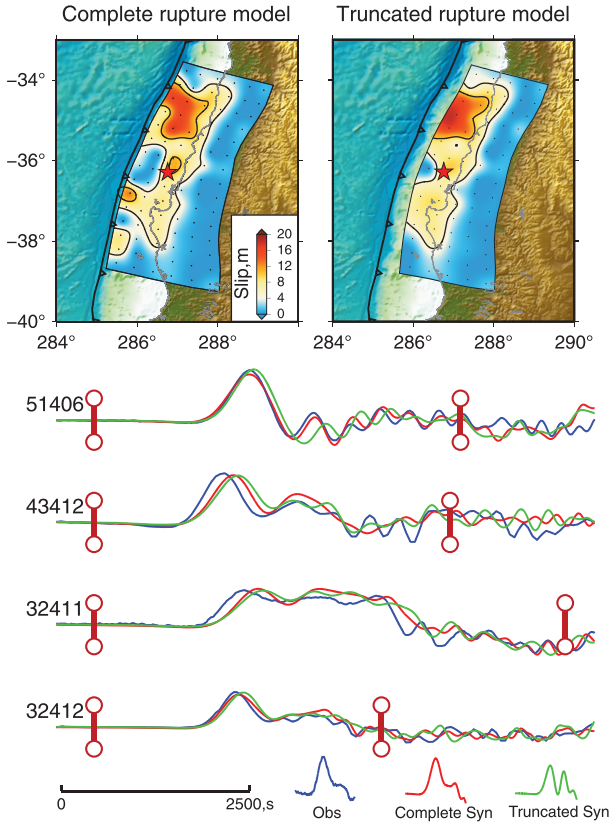

Figure 9. Inversion results using complete and truncated fault models are shown at the top. All parameters are identical in these inversions, except the shallowest row of subfaults is removed in the truncated fault model. Both models are plotted with the same color scale. Corresponding computed tsunami waveforms are plotted in red and green below, compared with the observed tsunami waveforms plotted in blue. The time window used in the joint inversion is bracketed by black bars. The timescale for all traces is indicated at the bottom.

spatial resolution of the overall rupture pattern. If no static data were available, this solution would need additional spatial smoothing to stabilize the rupture pattern.

The inversion result omitting the tsunami data set has amplified slip near the trench, which initially seems surprising. As discussed before, any near-trench rupture has very low excitation for seismic waves and near-field ground displacements, so shallow slip lies in the null space of the inversion and tends to produce unstable results if no data constrain it. This effect could be compensated by using a strong smoothing, but the model is then vulnerable to misinterpretation of whether there is shallow slip or not. In our prior work, we have conducted iterative modeling of tsunami data to reconcile joint inversions of other data types with the tsunami signals [e.g., *Lay et al.*, 2011a; *Yamazaki et al.*, 2011; *Yue et al.*, 2014], essentially penetrating into the null space of the inversion with a priori constraints provided by fitting the tsunami signals. Here including the tsunami data in the joint inversion directly intrinsically stabilizes the slip estimation near the trench.

To further test the robustness of the shallow slip patches, an inversion was performed in which the shallowest model row was removed. All other inversion parameters are the same as for the preferred model. The resulting slip model is shown in Figure 9, compared with the complete fault plane model. The along-strike slip distribution is not significantly impacted by truncation of the top model row, but the inverted slip on the second row is enhanced to compensate. The fault model truncation does not significantly degrade the data fits for the hr-GPS, teleseismic, and InSAR data sets, as expected based on the checkerboard tests (Figure 5). However, the truncation degrades the fit to the tsunami waveforms. This is shown in Figure 9, where waveforms predicted by the complete and truncated fault models are compared with the observations. The truncated fault model predicts slightly delayed waveforms that increase the mismatch of the initial arrival of the observed tsunami waves, but the amplitudes have minor affect. This effect is expected because the slip in the second row is enhanced for the truncated model, allowing the tsunami amplitude to still be matched, but the timing cannot be accounted for. The northern near-trench slip contributes significantly to the initial arrival of the main peak, and this is not fit well by the truncated model. The most significant degradation of waveform fitting is for station 51406, for which the second peak is not fit by the truncated model. As shown previously, this second peak is generated by the southern near-trench slip, which is missed in the truncated model.

Comparisons of our joint rupture model for the 2010 Maule event with results of other studies are shown in Figure 10. *Koper et al.* [2012] inverted teleseismic body waves; *Moreno et al.* [2012] inverted InSAR and campaign GPS statics; *Lorito et al.* [2011] inverted InSAR and tsunami data; *Delouis et al.* [2010] inverted hr-GPS, InSAR, and teleseismic body waves, and obtained good fits to teleseismic R_1 source time functions. Other models based on geodetic inversions, e.g., *Tong et al.* [2010], *Pollitz et al.* [2011], *Vigny et al.* [2011], and *Lin et al.* [2013], were compared but are not shown here because their results are generally similar to the model of *Moreno et al.* [2012].

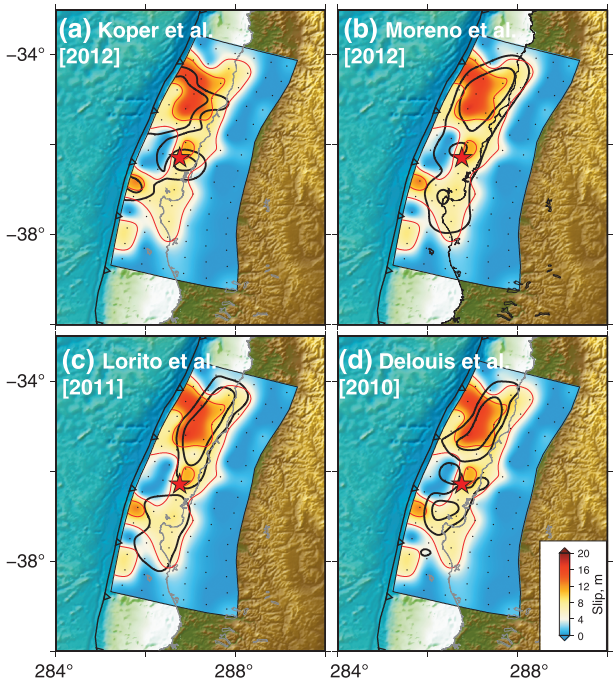

Figure 10. Comparison of slip models for the preferred joint inversion model and other finite-fault models. The preferred rupture model is plotted with blue-red color scale with 5 m and 10 m slip contours plotted in red. The 5 m and 10 m slip contours of other models are plotted in black in each panel. (a) The rupture model of *Koper et al*. [2012] was inverted using teleseismic *P* and *SH* waves. (b) The rupture model of *Moreno et al*. [2012] was inverted using campaign GPS and InSAR data sets. (c) The rupture model of *Lorito et al*. [2011] was inverted with InSAR and tsunami observations. (d) The rupture model of *Delouis et al*. [2010] was inverted with hr-GPS, teleseismic body waves, and InSAR data sets.

The geodesy-based inversions have similar along-strike slip patterns, but there are differences in the along-dip slip distributions. In the inversions of *Tong et al*. [2010], *Pollitz et al*. [2011], and *Lin et al*. [2013], there is no significant slip near the trench. However, the rupture model of *Moreno et al*. [2012] has ~5 m of slip near the trench in the north, as does the solution of *Vigny et al*. [2011], in the vicinity of our shallow slip patch. The larger slip in our model is almost invisible to the geodetic observations and likely is mapped into a broadened region of large slip in the northern slip patch in the geodetic-only inversions.

The teleseismic body wave inversions of *Lay et al*. [2010] and *Koper et al*. [2012] (Figure 9) are the only prior models that indicate more than 10 m of slip near trench. The teleseismic models differ primarily in their choice of rupture velocity, with the slip distribution expanding proportional to the assumed velocity. The slip distribution in our preferred model is more distributed than in that of *Koper et al*. [2012], due to the constraints from InSAR and hr-GPS observations. In the model of *Koper et al*. [2012] the slip near the trench is more smeared, similar to our regularized checkerboard test, and our joint model resolves more along-strike variation in the near-trench row. Our model has very little slip updip of the hypocenter, which is consistent with prior geodetic and seismic models, but appears to be less affected by inversion smoothing.

Lorito et al. [2012] and *Fujii and Satake* [2013] included tsunami records in their inversions, but their models do not place significant slip near the trench. Many of the tsunami records analyzed by *Lorito et al*. [2012] are tide-gauge recordings, which require very detailed near coast bathymetry models for accurate modeling, and those stations along the Chilean coast are not as sensitive to slip near the trench as the deep-water DART observations. *Lorito et al*. [2012] use the same software (COMCOT) to compute their tsunami Green functions as we use here but did not apply velocity correction to the calculated Green's functions. As discussed above the uncorrected tsunami Green function is expected to have ~1% early arrival times. For the typical epicentral distance (5000 km) of the DART observations in this study, a 1% velocity overestimation will lead to a 1% (50 km) epicentral distance overestimation, which shifts the centroid location of slip toward the land correspondingly. We performed an inversion using uncorrected tsunami Green's functions with all other data and parameters being the same as our preferred model. A comparison of the resulting slip distribution with our preferred result is shown in Figure 11, along with the tsunami waveform fitting. For the uncorrected tsunami Green functions, the predicted waveforms (green) show early arrivals even with slip shifted downdip, particularly for stations 51406 and 43412. Almost no slip is found in the shallowest row for this model. *Fujii and Satake* [2013] used the same deep ocean records as we do, together with regional tidal gauge observations. They adopted a finite difference method, solving linear shallow water equations [*Satake*, 1995], in which the velocity correction factors mentioned in this study are not included. Their simulations fit the arrival times at the relatively close DART stations well, with slip located below the coastline, which would occur in our uncorrected inversions if we used only the tsunami data. More distant tsunami observations

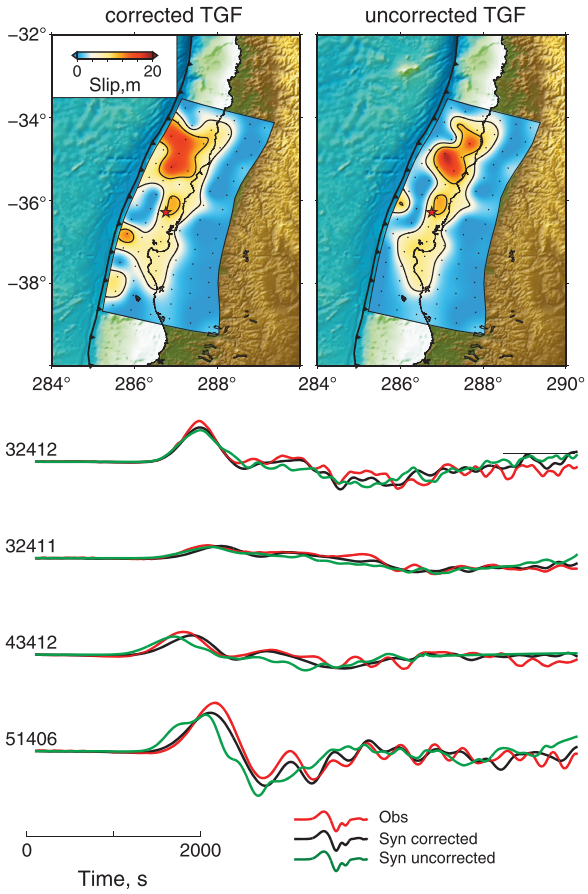

Figure 11. Inversion results obtained using corrected and uncorrected tsunami Green's functions are shown in the top panels. In each figure, the rupture pattern is plotted with a blue to red color scale. The epicenter location is marked with a red-filled star. Grid points in the rupture model are plotted with black dots. Comparisons of the observed and modeled tsunami waves are plotted in the bottom panels. The observed and modeled tsunami waves with corrected and uncorrected Green functions are plotted in red, black, and green curves, respectively.

across the Pacific are not well matched in timing by *Fujii and Satake* [2013]. Our conclusion is that errors in the tsunami Green functions can negate the value of deep-water tsunami observations for resolving shallow slip, so it is essential to apply corrections as we do in our preferred model.

Comparisons of our preferred rupture model with aftershock characteristics from the GCMT catalog and National Earthquake Information Center (NEIC) bulletin are shown in Figure 12. The GCMT catalog provides focal mechanisms for larger events, probably complete for $M_w \geq 5.0$. For this region the GCMT centroid locations are generally consistent with aftershock relocations using local seismic networks [*Lange et al*., 2012], so we plot the best double-couple mechanisms at the centroid locations. The GCMT events have a striking complementary distribution with the coseismic rupture pattern. The majority of thrusting aftershocks consistent with rupture of the plate interface are located in low-slip regions of the coseismic rupture. The low-slip region updip from the hypocenter has concentrated thrust aftershock activity, suggesting that it is not a locked zone that would be likely to rupture in a large tsunami earthquake in the near future. The margins of regions of thrust aftershocks are quite well defined by the 5 m slip contour of the rupture model. Few large interplate aftershocks are found in areas of large slip, including the wide area of the northern rupture patch and the more localized southern rupture area. Both large-slip areas define gaps in aftershock distribution. Larger thrust aftershocks also distribute outside the coseismic slip zone to the north and south. Few thrust aftershocks are located downdip from our coseismic rupture model, and this region has significant afterslip reported by *Lin et al*. [2013], indicating predominance of downdip creep. The lack of large thrust aftershocks within the shallow coseismic large-slip areas may be consistent with near complete stress release. The complementary distribution of large interplate aftershock events and the coseismic slip pattern was reported in previous studies [*Agurto et al*., 2012; *Hayes et al*., 2013], which used local networks to produce more complete and accurate aftershock catalogs. *Agurto et al*. [2012] compared the relocated interplate aftershocks with a geodesy-based rupture model and found aftershocks were concentrated near the margin of the coseismic rupture patches. However, because large near-trench slip is not resolved in the geodesy-based rupture model, the absence of near-trench aftershocks, updip from the main rupture pattern, is not well supported by their rupture model. Our rupture model, with enhanced near-trench slip, indicates an even more robust complementary pattern with the aftershock distributions. The GCMT catalog is only complete for $M_w > 5.0$ events, but the larger aftershocks in the relocated catalogs [*Agurto et al*., 2012; *Hayes et al*., 2013] generally have similar patterns to the GCMT catalog.

Two clusters of outer-rise normal faulting events are identified near 35°S and 38°S, located seaward along the plate motion direction relative to the regions of large near-trench slip. Outer-rise normal faulting has been particularly extensive for several large earthquakes that rupture to the trench and for tsunami earthquakes that

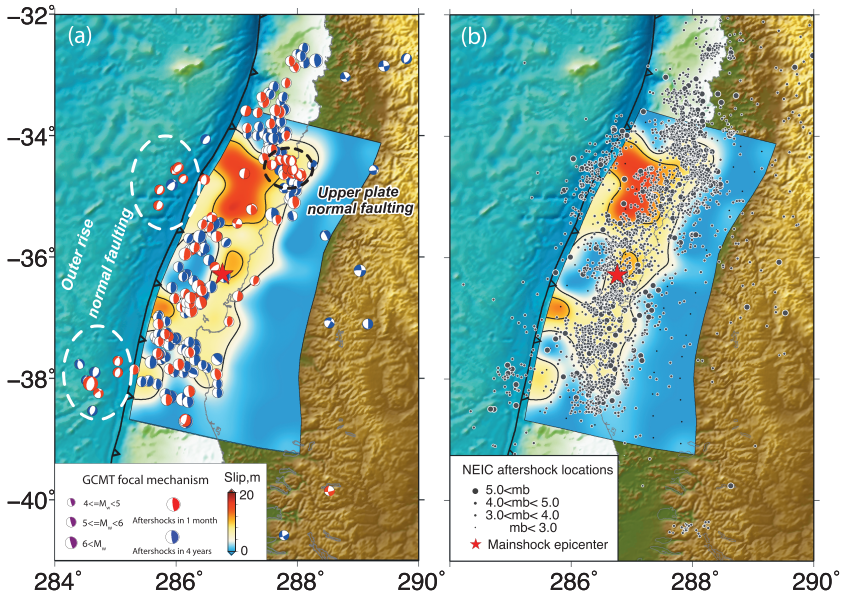

Figure 12. (a) Focal mechanisms from the GCMT catalog are superimposed on the preferred rupture model. Aftershocks within and after the first month following the main shock are plotted in red and blue, respectively. Focal mechanisms are scaled by their moment magnitude (M_w) with the scale shown in the legend. Two clusters of outer-rise normal faulting and one cluster of crustal normal faulting in the upper plate are outlined with white- and black-dashed circles. (b) Aftershock epicenters from the NEIC catalog are plotted with black-filled circles, with size scaled by the body wave magnitude (m_b). In both figures, the main shock epicenter is marked with a red-filled star.

do the same. The bending of the subducting plate is expected to cause extensional faulting and horst and graben formation perpendicular to the plate convergence direction, accounting for trench slope normal faulting at shallow depth in the subducting plate [e.g., *Lay et al*., 2009, 2011c; *Bilek et al*., 2011; *Yue et al*., 2014]. Very shallow coseismic slip appears to be particularly effective at triggering outer-rise normal faulting seaward of the shallow slip region.

Another cluster of shallow normal faulting is apparent landward of the peak coseismic slip in the northern part of the model (Figure 12). These events, relocated by *Lange et al*. [2012] and *Rietbrock et al*. [2012] and termed the Pichilemu seismic sequence [*Farías et al*., 2011], are mostly located in the crust of the upper plate and are likely induced by the concentrated dilatation stress change caused by the large-slip patch [*Ryder et al*., 2012; *Farías et al*., 2011]. This zone of normal faulting was not active prior to the 2010 Maule event, consistent with a compressional environment before the main shock.

The NEIC catalog locations for aftershocks are also plotted in Figure 12. This includes many smaller earthquakes with $m_b < 4$, a large percentage of which locate in the crust of the overriding plate. The NEIC catalog thus has a different pattern from the GCMT catalog, with activity overlying the coseismic large-slip area along the coast. The shallow microseismicity may indicate damage to the upper plate caused by coseismic rupture or a complex pattern of coseismic stress adjustment [*Lange et al*., 2012].

The slip distribution near the toe of the sedimentary prism during a large earthquake plays an important role in the tsunami generation and subsequent seismic hazard. If the rupture does not reach the trench, the possibility of a tsunami event in the future is raised, or the strain may be released in aseismic creep. The frictional stability of the shallowest portion of the megathrust has long been viewed as velocity strengthening with a well-defined seismic front, but that assumption is challenged by the observation of coseismic rupture reaching the trench for the 2011 Tohoku earthquake and the occurrence of a tsunami earthquake which ruptured along the toe of the sedimentary wedge along the Sunda trench after the 12 September 2007 M_w 8.5 and 7.9 Benkulu-Mentawai earthquake sequence [*Konca et al*., 2008]. The slip distribution resolved by the geodetic observations on the Mentawai islands, within ~100 km from the trench, establishes that no coseismic slip during the 2007 events reached the trench, an area that ruptured 3 years later in the 2010 M_w = 7.8 Mentawai tsunami earthquake. Concern about this possibility for the 2010 Maule

rupture zone appears to be reduced given the large amount of slip that did reach the trench seaward of large-slip patches on the deeper megathrust, along with the intensive thrust faulting aftershock activity in the region that did not have large shallow coseismic slip. This suggests that the potential for a tsunami earthquake along this region of the subduction zone is not high.

4. Conclusions

Performing joint inversion, using regional hr-GPS, teleseismic body waves, InSAR, campaign GPS, and tsunami observations, we obtain a robust and detailed rupture model of the 2010 Maule earthquake. The along strike-slip distribution shows a bilateral rupture pattern, dominated by northward rupture, which is consistent with previous studies. The resolution of slip near the trench is enhanced by the tsunami data set. In our preferred rupture model, significant slip (>12 m) was resolved at shallow depth in two major rupture patches. It is shown that correcting tsunami Green's functions for effects of mantle elasticity and water density is important for resolving the along-dip rupture pattern. The near-trench rupture is consistent with the clustering of normal faulting in the outer-rise direction. The significant shallow slip, combined with intensive thrust faulting aftershock activity in the region that did not have large shallow coseismic slip, reduces the potential for a tsunami earthquake in the future. The coseismic slip pattern shows a clear complementary relationship with large interplate thrusting aftershocks. The lack of large thrust aftershocks within the shallow coseismic large-slip areas, combined with the activation of extensive offshore normal faulting, is consistent with near complete stress release in localized regions of the shallow megathrust.

Acknowledgments

This work made use of GMT, SAC, and Matlab software. The IRIS data management center was used to access the seismic data from Global Seismic Network and Federation of Digital Seismic Network stations. DART buoy data were obtained from the NOAA National Data Buoy Center. We thank the Associate Editor and reviewers Marcos Moreno and Gavin Hayes for their valuable comments and suggestions. This work was supported in part by NSF grant EAR1245717 (T.L.).

References

Agurto, H., A. Rietbrock, I. Ryder, and M. Miller. (2012), Seismic-afterslip characterization of the 2010 M_w 8.8 Maule, Chile, earthquake based on moment tensor inversion, *Geophys. Res. Lett.*, *39*, L20303, doi:10.1029/2012GL053434.

Angermann, D., J. Klotz, and C. Reigber (1999), Space-geodetic estimation of the Nazca-South America Euler vector, *Earth Planet. Sci. Lett.*, *171*(3), 329–334, doi:10.1016/S0012-821X(99)00173-9.

Beck, S., S. Barrientos, E. Kausel, and M. Reyes (1998), Source characteristics of historic earthquakes along the central Chile subduction zone, *J. South Am. Earth Sci.*, *11*, 115–129.

Bedford, J., M. Moreno, J. C. Baez, D. Lange, F. Tilmann, M. Rosenau, and C. Vigny (2013), A high-resolution, time-variable afterslip model for the 2010 Maule M_w = 8.8, Chile megathrust earthquake, *Earth Planet. Sci. Lett.*, *383*, 26–36, doi:10.1016/j.epsl.2013.09.020.

Bilek, S. L., E. R. Engdahl, H. R. DeShon, and M. El Hariri (2011), The 25 October 2010 Sumatra tsunami earthquake: Slip in a slow patch, *Geophys. Res. Lett.*, *38*, L14306, doi:10.1029/2011GL047864.

Compte, D., A. Eisenberg, E. Lorac, M. Pardo, L. Ponce, R. Saragoni, S. K. Singh, and G. Suarez (1986), The 1985 central Chile earthquake: A repeat of previous great earthquakes in the region?, *Science*, *233*, 449–453.

Cubas, N., J.-P. Avouac, P. Souloumiac, and Y. Leroy (2013), Megathrust friction determined from mechanical analysis of the forearc in the Maule earthquake area, *Earth Planet. Sci. Lett.*, *381*, 92–103, doi:10.1016/j.epsl.2013.07.037.

Delouis, B., J.-M. Nocquet, and M. Vallée (2010), Slip distribution of the February 27, 2010 M_w = 8.8 Maule earthquake, central Chile, from static and high-rate GPS, InSAR, and broadband teleseismic data, *Geophys. Res. Lett.*, *37*, L17305, doi:10.1029/2010GL043899.

Farías, M., D. Comte, S. Roecker, D. Carrizo, and M. Pardo (2011), Crustal extensional faulting triggered by the 2010 Chilean earthquake: The Pichilemu seismic sequence, *Tectonics*, *30*, TC6010, doi:10.1029/2011TC002888.

Fujii, Y., and K. Satake (2013), Slip distribution and seismic moment of the 2010 and 1960 Chilean earthquakes inferred from tsunami waveforms and coastal geodetic data, *Pure Appl. Geophys.*, *170*, 1493–1509, doi:10.1007/s00024-012-0524-2.

Fujiwara, T., S. Kodaira, T. No, Y. Kaiho, N. Takahashi, and Y. Kaneda (2011), The 2011 Tohoku-Oki earthquake: Displacement reaching the trench axis, *Science*, *334*, 1240, doi:10.1126/science.1211554.

Haberland, C., A. Rietbrock, D. Lange, K. Bataille, and T. Dahm (2009), Structure of the seismogenic zone of the southcentral Chilean margin revealed by local earthquake traveltime tomography, *J. Geophys. Res.*, *114*, B01317, doi:10.1029/2008JB005802.

Hartzell, S. H., and T. H. Heaton (1983), Inversion of strong ground motion and teleseismic waveform data for the fault rupture history of the 1979 Imperial Valley, California, earthquake, *Bull. Seismol. Soc. Am.*, *73*(6A), 1553–1583.

Hayes, G. P., E. Bergman, K. L. Johnson, H. M. Benz, L. Brown, and A. S. Meltzer (2013), Seismotectonic framework of the 2010 February 27, 2010 M_w 8.8 Maule, Chile earthquake sequence, *Geophys. J. Int.*, *195*, 1034–1051, doi:10.1093/gji/ggt238.

Kido, M., Y. Osada, H. Fujimoto, R. Hino, and Y. Ito (2011), Trench-normal variation in observed seafloor displacement associated with the 2011 Tohoku-Oki earthquake, *Geophys. Res. Lett.*, *38*, L24303, doi:10.1029/2011GL050057.

Kikuchi, M., H. Kanamori, and K. Satake (1993), Source complexity of the 1988 Armenian earthquake: Evidence for a slow after-slip event, *J. Geophys. Res.*, *98*, 15–797, doi:10.1029/93JB01568.

Konca, A. O., et al. (2008), Partial rupture of a locked patch of the Sumatra megathrust during the 2007 earthquake sequence, *Nature*, *456*, 631–635, doi:10.1038/nature07572.

Koper, K. D., A. R. Hutko, T. Lay, and O. Sufri (2012), Imaging short-period seismic radiation from the 27 February 2010 Chile (M_W 8.8) earthquake by back-projection of P, PP, and PKIKP waves, *J. Geophys. Res.*, *117*, B02308, doi:10.1029/2011JB008576.

Kozdon, J. E., and E. M. Dunham (2014), Constraining shallow slip and tsunami excitation in megathrust ruptures using seismic and acoustic waves recorded on ocean-bottom sensor networks, *Earth Planet. Sci. Lett.*, *396*, 56–65, doi:10.1016/j.epsl.2014.04.001.

Lange, D., et al. (2012), Aftershock seismicity of the 27 February 2010 M_w 8.8 Maule earthquake rupture zone, *Earth Planet. Sci. Lett.*, *317–318*, 413–425, doi:10.1016/j.epsl.2011.11.034.

Lay, T. (2011), Earthquakes: A Chilean surprise, *Nature*, *471*(7337), 174–175, doi:10.1038/471174a.

Lay, T., H. Kanamori, and L. Ruff (1982), The asperity model and the nature of large subduction zone earthquakes, *Earthquake Pred. Res.*, *1*, 3–71.

Lay, T., H. Kanamori, C. J. Ammon, A. R. Hutko, K. Furlong, and L. Rivera (2009), The 2006-2007 Kuril Islands great earthquake sequence, *J. Geophys. Res.*, *114*, B113208, doi:10.1029/2008JB006280.

Lay, T., C. J. Ammon, H. Kanamori, K. D. Koper, O. Sufri, and A. R. Hutko (2010), Teleseismic inversion for rupture process of the 27 February 2010 Chile (M_w 8.8) earthquake, *Geophys. Res. Lett.*, *37*, L13301, doi:10.1029/2010GL043379.

Lay, T., C. J. Ammon, H. Kanamori, Y. Yamazaki, K. F. Cheung, and A. R. Hutko (2011a), The 25 October 2010 Mentawai tsunami earthquake (M_w 7.8) and the tsunami hazard presented by shallow megathrust ruptures, *Geophys. Res. Lett.*, *38*, L06302, doi:10.1029/2010GL046552.

Lay, T., C. J. Ammon, H. Kanamori, L. Xue, and M. J. Kim (2011b), Possible large near-trench slip during the 2011 M_w 9.0 off the Pacific coast of Tohoku earthquake, *Earth Planets Space*, *63*(7), 687–692, doi:10.5047/eps.2011.05.033.

Lay, T., C. J. Ammon, H. Kanamori, M. J. Kim, and L. Xue (2011c), Outer trench-slope faulting and the 2011 M_w 9.0 off the Pacific coast of Tohoku earthquake, *Earth Planets Space*, *63*(7), 713–718, doi:10.5047/eps.2011.05.006.

Lin, Y. N. N., et al. (2013), Coseismic and postseismic slip associated with the 2010 Maule Earthquake, Chile: Characterizing the Arauco Peninsula barrier effect, *J. Geophys. Res. Solid Earth*, *118*, 3142–3159, doi:10.1002/jgrb.50207.

Lorito, S., F. Romano, S. Atzori, X. Tong, A. Avallone, J. McCloskey, M. Cocco, E. Boschi, and A. Piatanesi (2011), Limited overlap between the seismic gap and coseismic slip of the great 2010 Chile earthquake, *Nat. Geosci.*, *4*(3), 173–177, doi:10.1038/ngeo1073.

Maeda, T., T. Furumura, S. Sakai, and M. Shinohara (2011), Significant tsunami observed at ocean-bottom pressure gauges during the 2011 off the Pacific coast of Tohoku earthquake, *Earth Planets Space*, *63*, 803–808, doi:10.5047/eps.2011.06.005.

Mei, C. C. (1989), *The Applied Dynamics of Ocean Surface Waves (Vol. 1)*, World Scientific. [Available at www.worldscientific.com.]

Miyazaki, S. I., J. J. McGuire, and P. Segall (2011), Seismic and aseismic fault slip before and during the 2011 off the Pacific coast of Tohoku earthquake, *Earth Planets Space*, *63*(7), 637, doi:10.5047/eps.2011.07.001.

Moreno, M., M. Rosenau, and O. Oncken (2010), 2010 Maule earthquake slip correlates with pre-seismic locking of Andean subduction zone, *Nature*, *467*, 198–202, doi:10.1038/nature09349.

Moreno, M., D. Melnick, M. Rosenau, J. Baez, J. Klotz, O. Oncken, and H. Hase (2012), Toward understanding tectonic control on the M_w 8.8 2010 Maule Chile earthquake, *Earth Planet. Sci. Lett.*, *321–322*, 152–165, doi:10.1016/j.epsl.2012.01.006.

Moreno, M. S., J. Bolte, J. Klotz, and D. Melnick (2009), Impact of megathrust geometry on inversion of coseismic slip from geodetic data: Application to the 1960 Chile earthquake, *Geophys. Res. Lett.*, *36*, L16310, doi:10.1029/2009GL039276.

Nishenko, S. P. (1991), Circum-Pacific seismic potential: 1989–1999, *Pure Appl. Geophys.*, *135*, 169–259.

Ohta, Y., et al. (2012), Quasi real-time fault model estimation for near-field tsunami forecasting based on RTK-GPS analysis: Application to the 2011 Tohoku-Oki earthquake (M_w 9.0), *J. Geophys. Res.*, *117*, B02311, doi:10.1029/2011JB008750.

Okada, Y. (1992), Internal deformation due to shear and tensile faults in a half-space, *Bull. Seismol. Soc. Am.*, *82*, 1018–1040.

Pollitz, F. F., et al. (2011), Coseismic slip distribution of the February 27, 2010 M_w 8.8 Maule, Chile earthquake, *Geophys. Res. Lett.*, *38*, L09309, doi:10.1029/2010GL047065.

Rietbrock, A., I. Ryder, G. Hayes, C. Haberland, D. Comte, S. Roecker, and H. Lyon-Caen (2012), Aftershock seismicity of the 2010 Maule M_w = 8.8, Chile, earthquake: Correlation between co-seismic slip models and aftershock distribution?, *Geophys. Res. Lett.*, *39*, L08310, doi:10.1029/2012GL051308.

Ryder, I., A. Rietbrock, K. Kelson, R. Bürgmann, M. Floyd, A. Socquet, C. Vigny, and D. Carrizo (2012), Large extensional aftershocks in the continental forearc triggered by the 2010 Maule earthquake, Chile, *Geophys. J. Int.*, *188*, 879–890, doi:10.1111/j.1365-246X.2011.05321.x.

Satake, K. (1995), Linear and nonlinear computations of the 1992 Nicaragua earthquake tsunami, in *Tsunamis: 1992–1994*, edited by F. Imamura and K. Satake, pp. 455–470, Birkhäuser, Basel.

Satake, K., Y. Fujii, T. Harada, and Y. Namegaya (2013), Time and space distribution of coseismic slip of the 2011 Tohoku earthquake as inferred from tsunami waveform data, *Bull. Seismol. Soc. Am.*, *103*, 1473–1492, doi:10.1785/0120120122.

Shimada, M., T. Tadono, and A. Rosenqvist (2010), Advanced Land Observing Satellite (ALOS) and Monitoring Global Environmental Change, *Proc. IEEE*, *98*(5), 780–799, doi:10.1109/JPROC.2009.2033724.

Simons, M., et al. (2011), The 2011 magnitude 9.0 Tohoku-Oki earthquake: Mosaicking the megathrust from seconds to centuries, *Science*, *332*, 1421–1425, doi:10.1126/science.1206731.

Tanioka, Y., and K. Satake (1996), Tsunami generation by horizontal displacement of ocean bottom, *Geophys. Res. Lett.*, *23*, 861–864, doi:10.1029/96GL00736.

Tassara, A., and A. Echaurren (2012), Anatomy of the Andean subduction zone: Three-dimensional density model upgraded and compared against global-scale models, *Geophys. J. Int.*, *189*, 161–168, doi:10.1111/j.1365-246X.2012.05397.x.

Tong, X., et al. (2010), The 2010 Maule, Chile earthquake: Downdip rupture limit revealed by space geodesy, *Geophys. Res. Lett.*, *37*, L24311, doi:10.1029/2010GL045805.

Tsai, V. C., J. P. Ampuero, H. Kanamori, and D. J. Stevenson (2013), Estimating the effect of Earth elasticity and variable water density on tsunami speeds, *Geophys. Res. Lett.*, *40*, 492–496, doi:10.1002/grl.50147.

Vigny, C., et al. (2011), The 2010 M_w 8.8 Maule mega-thrust earthquake of Central Chile, monitored by GPS, *Science*, *332*, 1417–1421, doi:10.1126/science.1204132.

Wang, R. (1999), A simple orthonormalization method for stable and efficient computation of Green's functions, *Bull. Seismol. Soc. Am.*, *89*, 733–741.

Wang, R., F. L. Martín, and F. Roth (2003), Computation of deformation induced by earthquakes in a multi-layered elastic crust—FORTRAN programs EDGRN/EDCMP, *Comput. Geosci.*, *29*, 195–207, doi:10.1016/S0098-3004(02)00111-5.

Watada, S., S. Kusumoto, and K. Satake (2014), Traveltime delay and initial phase reversal of distant tsunamis coupled with the self-gravitating elastic Earth, *J. Geophys. Res. Solid Earth*, *119*, 4287–4310, doi:10.1002/2013JB010841.

Yamazaki, Y., T. Lay, K. F. Cheung, H. Yue, and H. Kanamori (2011), Modeling near-field tsunami observations to improve finite-fault slip models for the 11 March 2011 Tohoku earthquake, *Geophys. Res. Lett.*, *38*, L00G15, doi:10.1029/2011GL049130.

Yamazaki, Y., K. F. Cheung, G. Pawlak, and T. Lay (2012), Surges along the Honolulu coast from the 2011 Tohoku tsunami, *Geophys. Res. Lett.*, *39*, L09604, doi:10.1029/2012GL051624.

Yue, H., and T. Lay (2011), Inversion of high-rate (1 sps) GPS data for rupture process of the 11 March 2011 Tohoku earthquake (M_w 9.1), *Geophys. Res. Lett.*, *38*, L00G09, doi:10.1029/2011GL048700.

Yue, H., and T. Lay (2013), Source rupture models for the M_w 9.0 2011 Tohoku earthquake from joint inversions of high-rate geodetic and seismic data, *Bull. Seismol. Soc. Am.*, *103*, 1242–1255, doi:10.1785/0120120119.

Yue, H., T. Lay, S. Y. Schwartz, L. Rivera, M. Protti, T. H. Dixon, S. Owen, and A. V. Newman (2013), The 5 September 2012 Nicoya, Costa Rica M_w 7.6 earthquake rupture process from joint inversion of high-rate GPS, strong-motion, and teleseismic *P* wave data and its relationship to adjacent plate boundary interface properties, *J. Geophys. Res. Solid Earth*, *118*, 5453–5466, doi:10.1002/jgrb.50379.

Yue, H., T. Lay, L. Rivera, Y. Bai, Y. Yamazaki, K. F. Cheung, E. M. Hill, K. Sieh, W. Kongko, and A. Muhari (2014), Rupture process of the 2010 M_w 7.8 Mentawai tsunami earthquake from joint inversion of near-field hr-GPS and teleseismic body wave recordings constrained by tsunami observations, *J. Geophys. Res. Solid Earth*, *119*, 5574–5593, doi:10.1002/2014JB011082.